

# Compression of floating ice fields

Mark A. Hopkins

U.S. Army Cold Regions Research and Engineering Laboratory, Hanover, New Hampshire

Jukka Tuhkuri

Ship Laboratory, Helsinki University of Technology, Espoo, Finland

**Abstract.** The compression of ice fields made up of thin floes is central to the processes of ice jam formation in northern rivers, pressure ridge formation in northern seas, and the dynamics of ice fields in Arctic and Antarctic marginal seas. This work describes the results of computer simulations in which a floating layer of circular floes, confined in a rectangular channel, is compressed by a pusher plate moving at a constant speed. The accuracy of the simulations is assessed by comparison with a series of similar physical experiments performed in a refrigerated basin. Following this comparison, the computer model is used to perform an extensive series of simulations to explore the effect of variations in channel length and width, the ratio of floe diameter to thickness, floe on floe friction coefficients, and the distribution of floe diameters on the force required to compress the floes. The results show that reducing the aspect ratio of the floes or increasing the friction coefficient increases the force needed to compress the floes. Both changes increase the force by changing the dominant failure mechanism in the layer of floes from rafting to overturning. Increasing channel width reduced the compressive force (per unit channel width) by reducing the relative importance of frictional drag at the channel edges. Last, the results of a simulation using a distribution of floe diameters was indistinguishable from those of a simulation using floes with a single diameter equal to the average diameter of the distribution.

## 1. Introduction

The compression of ice fields made up of thin floes is central to the processes of ice jam formation in northern rivers, pressure ridge formation in northern seas, and the dynamics of ice fields in Arctic and Antarctic marginal seas. Breakup ice jams form from an intact ice cover broken into floes by river surges. Freeze-up ice jams form from circular ice pans grown from frazil ice. Ice jams occur at river bends, constrictions, and at points of abrupt decrease in river slope. In northern seas, pressure ridges form from fragmented ice fields compressed by divergence of the wind field, inertia, or an onshore wind, which drives the floes against the beach or landfast ice. In Arctic and Antarctic marginal seas the presence of waves and frazil ice causes the formation of circular pancake ice. Onshore winds herd the ice pans against the coast or the landfast ice. Once an ice jam, pressure ridge, or rubble field has been initiated, subsequent thickening and growth under continued compression depends on the dynamics of the ice floe accumulation.

Ice jam and rubble thickening were first represented in numerical models by assuming a passive pressure coefficient to characterize ice rubble strength [Pariset *et al.*, 1966; Uzuner and Kennedy, 1976]. Recently, discrete element models (DEM) have been used to simulate deformation processes occurring in sea and river ice. In-plane deformation of circular floes has been simulated using two-dimensional DEMs by Babic *et al.* [1990], Hopkins and Hibler [1991], Loset [1994], and Sayed *et al.* [1994]. Pressure ridge formation from compression of a field of

ice floes has been studied using two-dimensional (vertical plane) DEMs by Hopkins *et al.* [1991]. However, in ice jams, pressure ridges, and rubble fields the strength of the ice accumulation depends on both out of plane thickening and interaction with lateral boundaries, which requires a three-dimensional model.

In this work we use a newly developed three-dimensional DEM, which uses disk-shaped floes [Hopkins *et al.*, 1996], to simulate the compression of a floating layer of circular ice floes confined within a rectangular channel. On one side the floes are compressed by a vertical plate moving at a constant speed. The forces exerted by the ice on the pusher are calculated at each time step. The results of the computer simulations are compared with results from similar physical model experiments performed in the refrigerated basin in the Ship Laboratory at the Helsinki University of Technology. The channel dimensions and important material parameters used in the simulation were measured from the model experiments. After verifying the simulation through direct comparison with model experiments, we did further simulations to determine the effects of variations in channel length, channel width, floe aspect ratio, friction coefficients, and distribution of floe diameters.

## 2. Mechanics of the Simulation

A discrete element model is a computer program that explicitly models the dynamics of a system of discrete particles. In these simulations the particles are the individual ice floes. The position, orientation, velocity and shape of each floe are stored in arrays. At each time step, the contact and body forces on each floe are calculated, and the floes are moved to new locations with new velocities that depend on the resultant of the

Copyright 1999 by the American Geophysical Union.

Paper number 1999JC900127.  
0148-0227/99/1999JC900127\$09.00

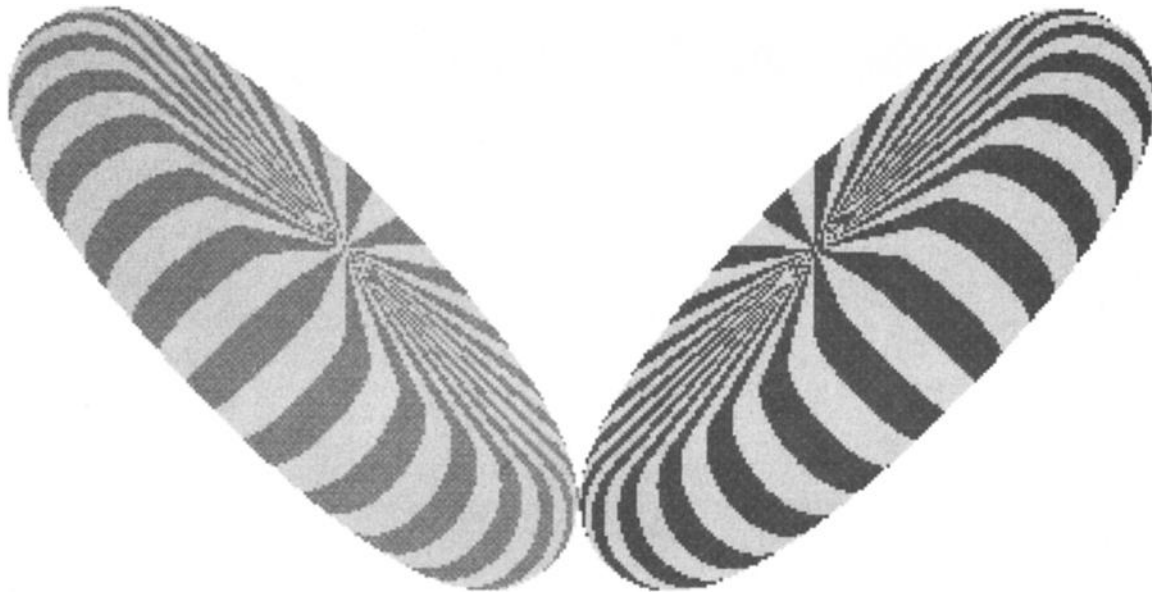


**Figure 1.** Edge on edge contact between two floes, characteristic of floe overturning.

forces. A detailed description of the mechanics of the simulation used in this work is given in *Hopkins et al.* [1996]. The important details are summarized here.

The ice floes in the simulations are flat disks with a circular edge as shown in Figure 1. The floes are formed by dilating a flat disk of radius  $R_1$  by a sphere with radius  $R_2$ . In the dilation process in mathematical morphology [Serra, 1986] the two-dimensional circular disk is transformed into a three-dimensional disk with thickness  $h = 2R_2$  and diameter  $d = 2(R_1 + R_2)$  by placing a sphere with radius  $R_2$  at every point on the two-dimensional circular disk. The aspect ratio of the floe  $d/h$  can be varied by changing  $R_1$  and  $R_2$ . The top and bottom surfaces of the floes are flat.

Contact detection, which is the crux of any discrete element code, is handled by a new iterative method. The two-dimensional circular disk of radius  $R_1$  at the core of each floe is called a constraint surface. The external surface of the floe is, at all points, a distance  $R_2$  from the constraint surface. When two disks are found to be in proximity (by standard grid methods), a vector is arbitrarily placed with its head on the constraint surface of one floe and its tail on the constraint surface of the other floe. This vector is modeled as an elastic band whose ends are constrained to remain on the two constraint surfaces. Pulled by its elasticity, the head and tail of the vector move iteratively to locations on the constraint surfaces that define the shortest distance between the two floes. If the length of the vector is less than  $R_2$ , then the floes are in contact. The

vector, which is perpendicular to the external surfaces of the two floes, defines the normal to the contact surface.

Two types of contact between a pair of floes are shown in Figures 1 and 2. The first type, shown in Figure 1, is a contact between two circular edges. This type of contact, in which the floes rotate downward, is characteristic of floe overturning. The second type, shown in Figure 2, is a contact between two flat surfaces. This type of contact, in which one floe slides over the other, is characteristic of floe rafting. A third type of contact between a circular edge and a flat surface is also modeled but not shown.

Wherever two floes touch, the overlap is interpreted as a deformation of the floes resulting in a contact force. The contact force has components normal and tangential to the surfaces at the point of contact. The normal axis  $\mathbf{n}$  is perpendicular to the surface of each floe. The tangential axis  $\mathbf{t}$  is in the direction of the tangential component of the relative velocity at the point of contact. The normal component of the contact force is

$$F_n^n = k_n \delta - \eta \mathbf{V}_{1/2} \cdot \mathbf{n} \quad (1)$$

The subscript  $n$  denotes the normal direction, the superscript  $n$  denotes the current time step,  $k_n$  is the normal contact stiffness,  $\delta$  is the depth of overlap between the floes,  $\eta$  is the normal contact viscosity, and  $\mathbf{V}_{1/2}$  is the relative velocity of floe 1 with respect to floe 2 at the point of contact. A value of  $\eta$  near critical damping is used to produce highly inelastic be-

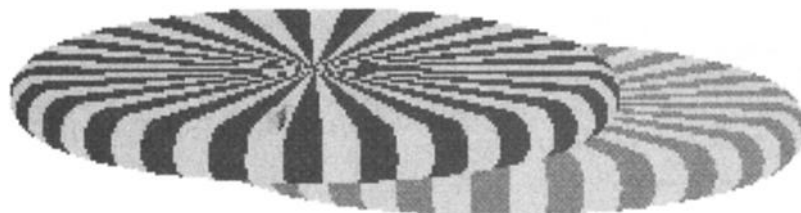


**Figure 2.** Flat surface on flat surface contact between two floes, characteristic of floe rafting.

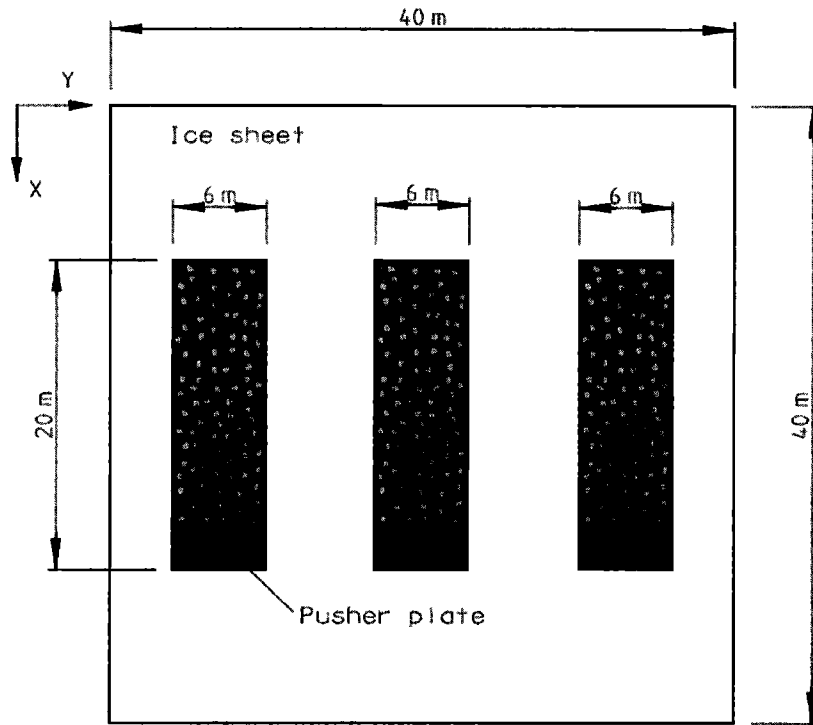


**Figure 3.** Layout of the model experiments in the Helsinki University of Technology (HUT) ice basin.

havior. Tensile forces are not modeled. The incremental change in the tangential force due to friction is proportional to the relative tangential velocity. The tangential force at time  $n$  is

$$\mathbf{F}_t^n = \mathbf{F}_t^{n-1} - k_t \Delta t (\mathbf{V}_{1/2} \cdot \mathbf{t}) \mathbf{t} \quad (2)$$

where  $\Delta t$  is the time step and  $k_t$  is the tangential contact stiffness that is set to 60% of  $k_n$ . The magnitude of  $k_t$  affects the rate at which the frictional force increases to the Coulomb limit  $\mu F_n$ , where  $\mu$  is the friction coefficient. If the tangential force  $F_t$  exceeds the Coulomb limit, the  $x$ ,  $y$ , and  $z$  components of  $F_t$  are scaled such that  $|F_t| = \mu F_n$ . The torques on each floe are calculated from the forces and moment arms. The water drag force  $F_d$  on a floe is given by

$$\mathbf{F}_d = -\frac{1}{2} C_d \rho_w A \mathbf{V} |\mathbf{V}| \quad (3)$$

where  $C_d$  is the drag coefficient,  $\rho_w$  is the water density, and  $A = \pi(R_1 + R_2)^2$  is the floe area. The drag force is separated into components normal and tangential to the flat surface of a floe. The drag coefficient  $C_d$ , based on floe area, is 1.17 for flow normal to the flat surface and 0.1 for flow tangential to the flat surface [White, 1979]. Rotational drag  $M_d$  on a floe is given by

$$M_d = -\frac{1}{2} C_d \rho_w A \omega |\omega| \quad (4)$$

where  $\omega$  is the rotational velocity. The rotational drag coefficient used in the simulations was 0.5. The water drag was applied only to the underwater floes that were in an exposed position. Floes in the interior of a moving mass of floes felt no drag. The buoyant force and its moment on each floe were also calculated. More complicated hydrodynamic effects, such as lift and added mass, were not modeled. In the simulations, water drag accounted for ~10% of the total energy expended.

After the sum of the forces and torques exerted on each floe has been calculated, the equations of motion for each floe are

solved and time is advanced. The translational equations of motion use simple central difference approximations. Changes in the angular velocities and orientation of the floes are much more complicated to calculate. We use a method developed by Walton and Braun [1993]. Euler's equations of motion for the time derivatives of the angular velocities in the principal body frame are solved using a predictor-corrector algorithm. Floe orientations are specified by four parameters called quaternions [Evans and Murad, 1977]. The updated quaternions are found by solving central-difference equations for the time derivatives of the quaternions, expressed in terms of the quaternions themselves and the angular velocities.

In each simulation the change in kinetic and potential energy of the floes, the energy dissipated by inelastic frictional contacts and water drag, and the work done by the pusher are calculated at each time step. Inelastic and frictional dissipation are determined by computing the work performed by the normal and tangential components of each contact force. These calculations are described by Hopkins [1994]. The energy balance is used to gauge numerical accuracy. In the simulations described in section 3, the error in the energy balance was <2%.

### 3. Model Experiments: Compression of Circular Ice Floes

A uniform sheet of model ice was grown in the 40 m × 40 m ice basin at the Ship Laboratory at the Helsinki University of Technology. Three 6 m × 20 m rectangular channels were defined by kerfs cut around their perimeters, as shown in Figure 3. Thirty percent of the ice in each channel was discarded. The remaining 70% was cut into identical floes, 400 mm in diameter. The floes were cut in close-packed hexagonal configuration. The triangular, interstitial pieces, roughly 10%

of the ice area, were retained. The floes were uniformly distributed over each rectangular channel. The floes in each channel were confined on three sides by the parent ice sheet and on the fourth side by a vertical pusher plate attached through load cells to a movable carriage (Figure 3).

In the experiments the pusher plate moved 17.8 m at a constant speed. A photograph of an experiment is shown in Figure 4, looking toward the channel end opposite the pusher. In the picture, two bands of rafting floes cross the channel. Amazingly, although ice strength was scaled, most of the floes survived the experiments intact. Nine experiments were performed with three carriage speeds (15, 33, and 52 mm s<sup>-1</sup>) and three ice thicknesses (28, 38, and 54 mm). The force on the pusher plate was measured by the load cells. The results, along with the results of similar experiments with square floes, are reported by *Tuhkuri and Lensu* [1997] and *Hansen and Tuhkuri* [1997]. The measured forces showed substantial differences due to thickness and nominal effects due to speed. The effect of variations in speed was attributed to the effects of speed on sliding friction.

Three further experiments were done to measure sliding friction. In each experiment a 3 m wide and 10 m long sheet of ice was pushed over a similar freely floating sheet in the longitudinal direction. The pushing force was measured and converted to an effective friction coefficient. Experiments at speeds of 16, 36, and 55 mm s<sup>-1</sup> yielded effective friction coefficients of 0.33, 0.32, and 0.12, respectively [*Tuhkuri and Lensu*, 1997].

#### 4. Comparison of Compression Experiments and Simulations

A parallel set of simulations were performed with the computer model described in section 3. The configuration of the simulations was as nearly similar to the model experiments as possible. There were two notable differences between the simulations and the experiments. As mentioned above, the experiments included the presence of the small triangular interstitial pieces that remained from cutting the circular floes in a close-packed hexagonal arrangement. The triangular pieces added ~10% to the ice volume in the channel. Since it was impossible for the computer program to model these pieces, extra circular floes were added to the simulations to bring the total area of ice up to the 84 m<sup>2</sup> of ice in the model tests. The second difference was that while circular floes cut from the ice sheet in the model experiments had vertical edges, the floes used in the simulations had circular edges. After comparing the results of the simulations and the experiments, it was apparent to us that the vertical edges impeded rafting. Furthermore, this effect increased with thickness. To compensate, separate friction coefficients were used in the simulations for contacts between circular edges and for contacts involving a flat surface. The flat surface friction coefficient  $\mu_s = 0.35$  was deduced from the results of the lower speed model experiments described above. The circular edge friction coefficient  $\mu_e$  was varied with ice thickness to approximate the effect of the vertical edges present in the model experiments. The parameters used in the simulations are listed in Table 1.

The time step  $\Delta t$  used in the simulations was equal to  $0.033\pi(m/k_n)^{1/2}$ , where  $m$  is the floe mass. The contact stiffness  $k_n$  is used to calculate the normal contact force in (1) between contacting floes. While the contact stiffness should ideally be related to Young's modulus, in a discrete element

simulation, since the time step is inversely proportional to the square root of  $k_n$ , a lower stiffness must sometimes be used in the interest of computational efficiency. At a minimum, the stiffness coefficient must be sufficiently large to make the overlaps during contact between neighboring floes negligible. The maximum contact forces in the present simulations were 25 N, corresponding to a maximum overlap of <1 mm using the value of  $k_n$  listed in Table 1.

During the simulations the force on the pusher plate was calculated at each time step. Contacts between the floes and the edges of the confining ice sheets used the friction coefficient  $\mu_s$ . Forces and profiles obtained in simulations performed at a pusher speed of 10 mm s<sup>-1</sup> showed no systematic differences when compared with those obtained at a speed of 50 mm s<sup>-1</sup>. The higher speed was used throughout this study in the interest of computational efficiency.

A snapshot from a simulation is shown in Figure 5. The thickened layer of floes moving ahead of the pusher is compressing the intact surface layer of floes on the left-hand side of Figure 5 causing it to fail in places. The simulation shown in Figure 5 used 663 floes, its duration was 350 s, and it required 120 min of CPU time on a 300 MHz Pentium II. The forces on the pusher plate obtained in the model experiments and simulations with two ice thicknesses are shown in Figure 6. The results of the model experiments were from tests performed at 33 mm s<sup>-1</sup> [*Hansen and Tuhkuri*, 1997]. The force  $F$ , displacement  $X$ , and channel length  $L$  were nondimensionalized in the following manner:

$$F^* = F/\rho_i g w h d \quad X^* = X/d \quad L^* = L/d \quad (5)$$

where  $\rho_i$  is the ice density,  $g$  is the gravitational acceleration,  $w$  is the channel width,  $h$  is the floe thickness, and  $d$  is the floe diameter. Displacement was measured at the leading edge of the pusher shown in Figure 5.

Three distinct regions are evident in the force-displacement plots in Figure 6. During the first period ( $X^* < 6$ ), the forces increase as the floes are herded toward the far end of the channel and the surface concentration of the floes in the channel increases. Little or no rafting or underturning takes place in this period. Following the period of initial consolidation, failure of the surface layer of floes by underturning (Figure 1) and rafting (Figure 2) begins in the vicinity of the pusher plate. The magnitude of the pusher force at his point ( $X^* \approx 6$ ) represents the strength of the consolidated surface layer of horizontal floes. With continued compression the failure zone spreads gradually toward the other end of the channel. This progression is shown in the series of five snapshots in Figure 7, looking edge on at the channel. No systematic lateral variation in thickness was evident in the simulation results. As the failure zone progresses from the area in front of the pusher toward the channel end, the force exhibits a slow, apparently linear increase. The thickness of the failure region is greatest at the pusher and decreases in the direction of the opposite end. When all of the ice in the initial surface layer has failed, the channel surface resembles a rubble field. Further movement of the pusher plate causes the rubble to thicken. This coincides with the rapid increase of the forces shown in Figure 6 when  $X^* > 35$ .

The first period ( $X^* < 6$  in Figure 6) can be called the consolidation phase. At the end of the consolidation phase the floes are packed together in a single layer on the surface at an average concentration of 79% by area. For comparison the highest concentration attainable in two-dimensions, a close-

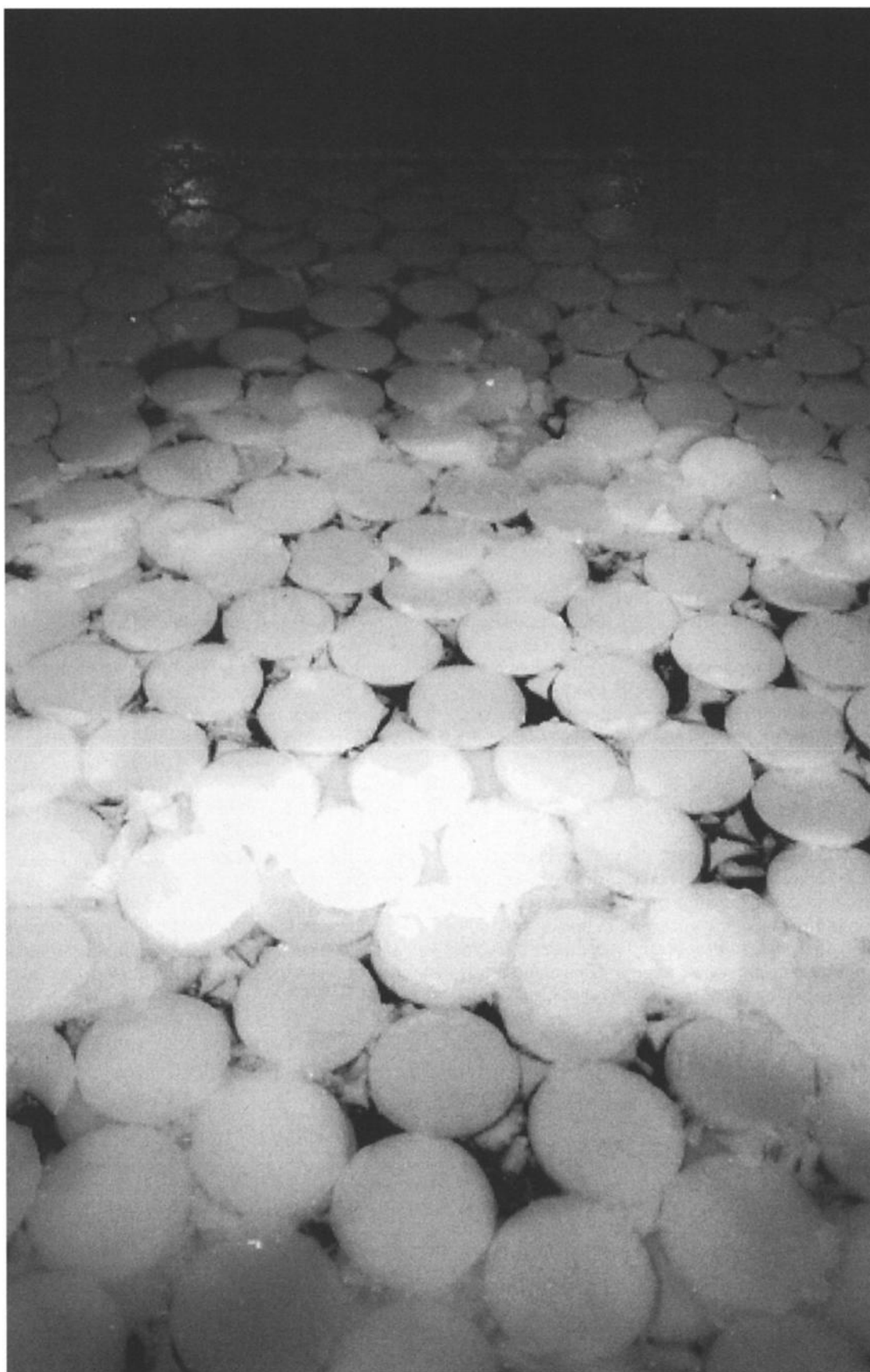


**Figure 4.** Experiment with 28 mm thick ice. At the top is the end of the channel opposite the pusher. Two bands of rafting floes cross the channel.

**Table 1.** Parameters Used in the Simulations

Parameter	Symbol	Value
Channel length, m	$L$	20
Channel width, m	$w$	6
Pusher speed, mm s <sup>-1</sup>		50
Floe thickness, mm	$h$	28, 54
Floe diameter, mm	$d$	400
Ice density, kg m <sup>-3</sup>	$\rho_i$	900
Water density, kg m <sup>-3</sup>	$\rho_w$	1000
Normal contact stiffness, kN m <sup>-1</sup>	$K_n$	50
Flat surface friction	$\mu_s$	0.35
Edge friction	$\mu_e$	0.5 ( $h = 28$ mm), 0.9 ( $h = 54$ mm)

packed hexagonal arrangement, has an areal concentration of 90.6%. The longitudinal force during consolidation arises from the inertia of the accelerating floes, increasing both water drag as more floes are set in motion and frictional contact with the channel edges.

The second period ( $6 < X^* < 35$  in Figure 6) is characterized by progressive failure of the consolidated ice cover, which spreads from the region in front of the pusher toward the opposite end of the channel. During failure the floes, which initially float horizontally at the water surface, overturn (Figure 1) and raft (Figure 2). The end result is a disordered layer of floes with a distribution of orientations. The second period is thus akin to a phase change from an initial ordered state of uniform orientation to a disordered state, in which floe orientations are more random. The longitudinal force during the second period is caused by the resistance of the surface layer of floes to overturning and rafting and to frictional contact with the channel edges.

The third period ( $X^* > 35$  in Figure 6) begins when the entire initial surface layer of floes has failed. During the third period, compression of the floes causes the layer of rubble to thicken. The longitudinal force during the third period is caused by the resistance of the rubble layer of floes to further compression and to frictional contact with the channel edges. If deformation is prolonged, the floes tend to line up vertically like books on a shelf. Because the computer model does not include failure mechanisms, such as floe breakage and crush-

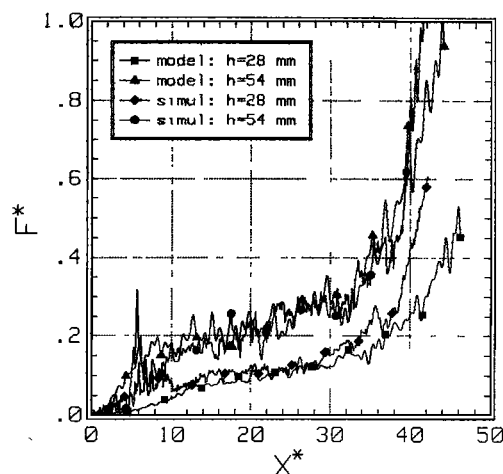


**Figure 6.** Comparison of pusher forces measured in simulation (simul) and model experiments. The force and displacement are nondimensional ( $L^* = 50$ ,  $d = 400$  mm,  $h = 54$  mm,  $\mu_e = 0.9$ , and  $\mu_s = 0.35$ ).

ing, the forces soon reach levels that are not realistic for ice floes. The simulations in this study were terminated well before this occurred.

During the second period the failure of the surface layer of floes begins in the vicinity of the pusher plate and spreads gradually toward the other end of the channel, as shown in Figure 7. This is because the longitudinal force in the layer of floes is highest at the pusher and decreases steadily toward the far end of the channel. The longitudinal force, as a function of longitudinal channel position, is shown in Figure 8 for six positions of the pusher plate. The forces shown were obtained by averaging the results of 10 simulations and smoothing to further reduce noise. The 10 simulations began with slightly different initial configurations.

The first plot, with the pusher at  $X^* = 6.3$ , corresponds to the initial failure of the surface layer of floes. Here the longitudinal force at the pusher is 3 times higher than the force at the far end. The gradient in the longitudinal force is caused by friction between the floes and the ice sheet on each side of the

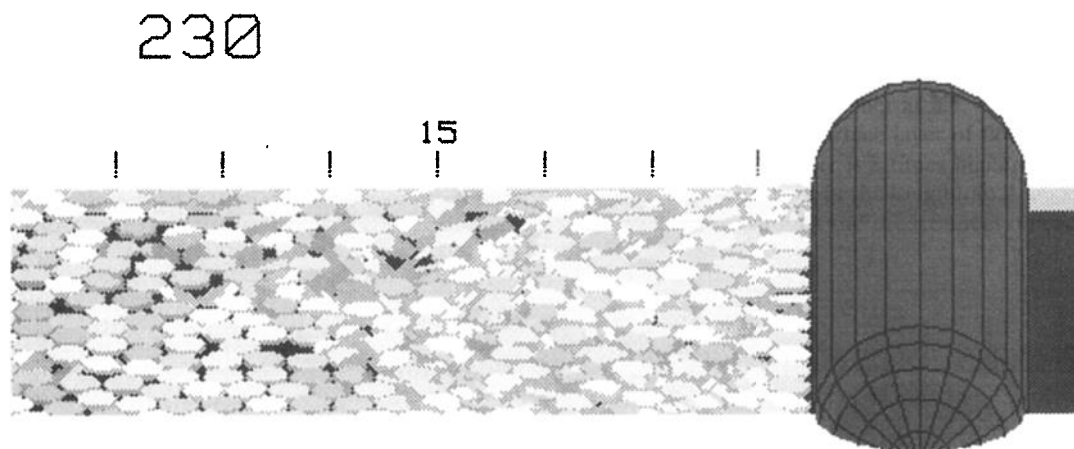


**Figure 5.** Snapshot from a simulation. The large cylinder to the right is the pusher. The distance markings on the far side of the channel are in meters (channel length  $L = 20$  m, diameter  $d = 400$  mm, thickness  $h = 54$  mm, circular edge friction coefficient  $\mu_e = 0.9$ , and flat surface friction coefficient  $\mu_s = 0.35$ ).

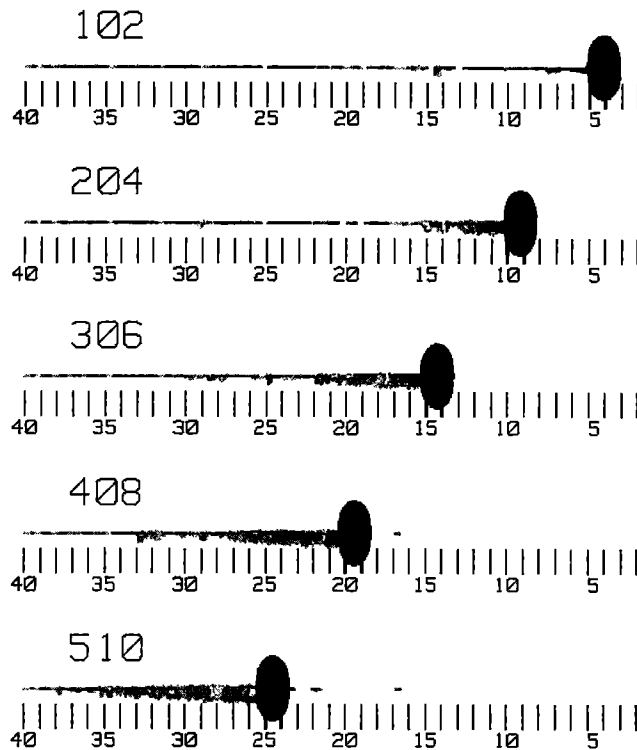


**Figure 7.** Sequential snapshots from a simulation. The large cylinder to the right is the pusher. The radius of the pusher is 1 m. The vertical scale has been doubled ( $L = 40$  m,  $d = 400$  mm,  $h = 54$  mm,  $\mu_e = 0.9$ , and  $\mu_s = 0.35$ ).

channel. All contacts between floes and the sheets at the sides of the channel used the friction coefficient  $\mu_s$ . The frictional force per unit length on the sides of the channel (the total of both sides), as a function of longitudinal channel position, is shown in Figure 9 for the same six positions of the pusher plate. In general, the frictional force is highest where the ice is in motion, namely in the ice moving with the pusher. This is

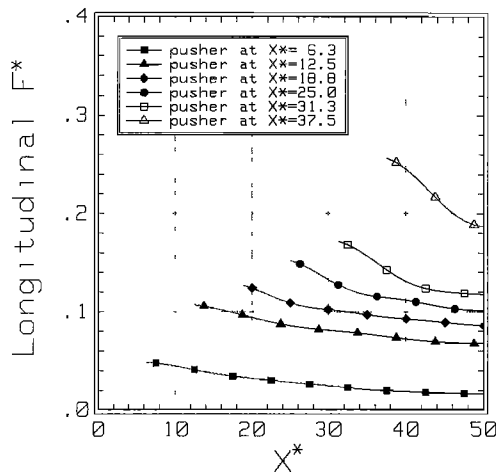


**Figure 8.** Nondimensional longitudinal force versus nondimensional longitudinal channel position for six different positions of the pusher plate ( $L^* = 50$ ,  $d = 400$  mm,  $h = 54$  mm, and  $\mu_e = \mu_s = 0.35$ ).

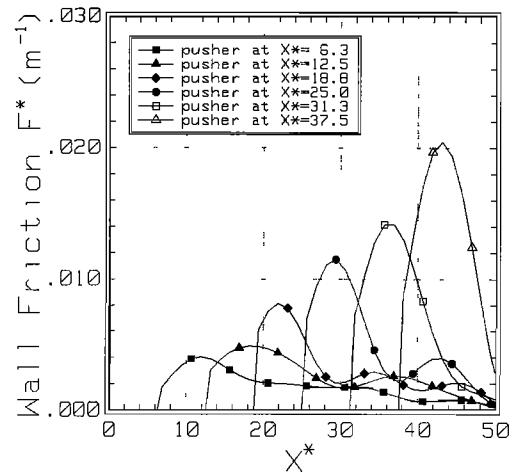


**Figure 9.** Nondimensional frictional force per unit length on the confining sheets versus nondimensional channel position for six different positions of the pusher plate ( $L^* = 50$ ,  $d = 400$  mm,  $h = 54$  mm, and  $\mu_e = \mu_s = 0.35$ ).

also the point where the rubble accumulation is thickest, as shown in Figure 7.

## 5. Further Simulations Exploring the Effects of Parameter Variations

In this section we use the computer model to perform simulations to determine the effect on graphs of nondimensional force versus displacement of variations in the length and width of the channel, the floe aspect ratio, friction coefficients, and the distribution of floe diameters.

### 5.1. Channel Length

As the pusher moves, the length of the rubble region moving with the pusher grows. This growth continues until the leading edge of the rubble accumulation reaches the far end of the channel. When this occurs, the force rises rapidly as shown in Figure 6 for  $X^* > 35$ . If the length of the channel is increased, while keeping initial floe concentration constant, then the rubble accumulation will continue to grow for a longer period before it reaches the far end. As the rubble accumulation grows in length, the frictional force on the walls grows, and the pusher force increases. This has the effect of lengthening the intermediate period of linear increase of the pusher force shown in Figure 6. The pusher forces versus displacement for channels with length  $L^* = 50$ , 100, and 200 are shown in Figure 10. It is apparent from Figure 10 that while the length of the linear region increases with channel length, its slope remains approximately the same.

### 5.2. Channel Width

Longitudinal force is a combination of the longitudinal pressure in the channel and the frictional force on the edges of the channel. The frictional force is caused by the lateral pressure on the edges, which is a function of longitudinal pressure. The effect of edge friction on the longitudinal force will diminish as channel width increases because although the longitudinal force grows with channel width, longitudinal pressure and edge friction remain roughly constant. The effect of channel width on the longitudinal force is shown in Figure 11. The diminishing effect of edge friction as channel width increases is shown

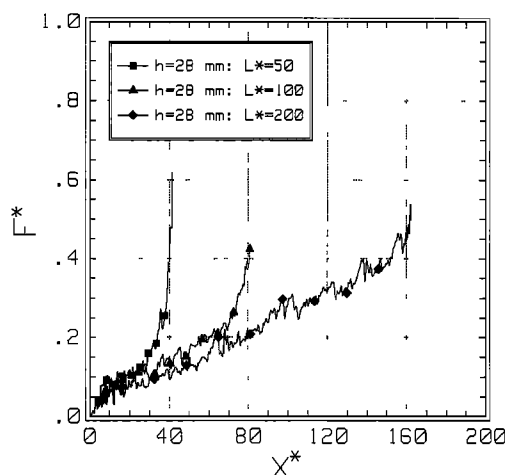


**Figure 10.** Nondimensional pusher force versus nondimensional pusher displacement for channel lengths  $L^* = 50$ , 100, and 200 (channel width  $w = 6$  m,  $h = 28$  mm,  $\mu_e = 0.5$ , and  $\mu_s = 0.35$ ).

by the decreasing slope in the central part of the graphs. In the region between nondimensional displacements of 6 and 30 the force increases most rapidly in the 3 m wide channel where edge effects are strongest. In the case where edge friction was eliminated by substituting periodic boundaries for edge sheets in a 6 m wide channel, the force hardly increases. Periodic boundaries are routinely used in discrete element simulations to eliminate solid boundaries [see, e.g., Hopkins and Louge, 1991]. In the absence of edge sheets the floes on the right boundary interact with the periodic image of the floes on the left boundary and vice versa.

In the channel with periodic boundaries the absence of edge friction causes the average pressure in the floe field to be uniform in the longitudinal direction. Because of this the floe field is no longer forced to fail in the vicinity of the pusher but is equally likely to fail anywhere in the channel. Furthermore, since the uniform longitudinal pressure in the channel is limited by the strength of the intact surface layer, the pusher force

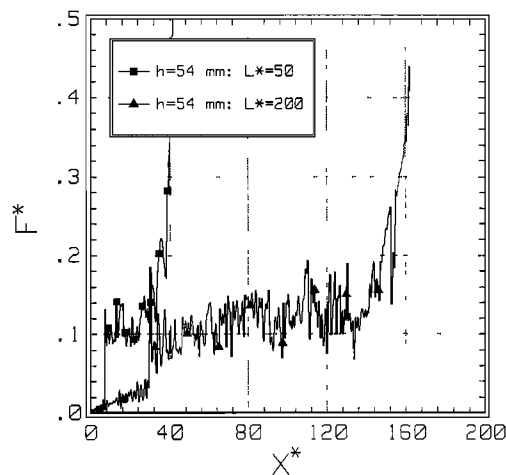


**Figure 12.** Nondimensional pusher force versus nondimensional pusher displacement for channel lengths  $L^* = 50$  and 200 with periodic lateral boundaries ( $w = 6$  m,  $h = 54$  mm, and  $\mu_e = \mu_s = 0.35$ ).

remains roughly constant until the intact surface layer is entirely consumed. This is shown in Figure 12, which compares simulations of two channels with length  $L^* = 50$  and 200.

### 5.3. Floe Aspect Ratio

The effect of varying the aspect ratio of the floes  $d/h$  is shown in Figure 13. In the simulations, floe diameter was held constant while the thickness was varied. In the central part of the force plots the pusher force varies inversely with the aspect ratio. That is, the thicker floes with lower aspect ratios engender higher forces than the thinner floes. The comparison is complicated by floe volume in the channel being proportional to the floe thickness. However, the expected increase in force due to the increase in floe volume is diminished, if not removed, when the force is divided by floe thickness in its nondimensionalization. The remaining effect of the aspect ratio is the result of a strengthening of the surface layer of horizontal floes because of increased thickness. This effect is visible at the

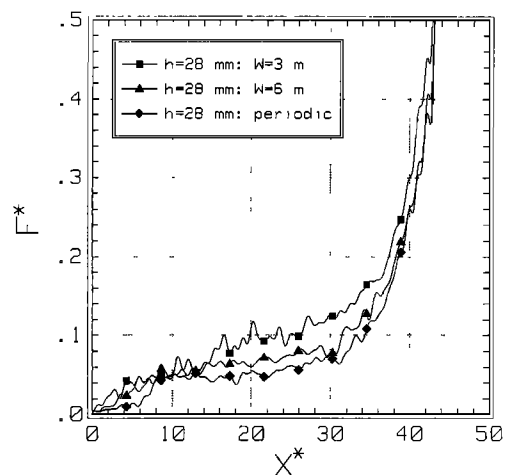


**Figure 11.** Nondimensional pusher force versus nondimensional pusher displacement for channel widths  $w = 3$  m, 6 m, and periodic ( $L^* = 50$ ,  $h = 28$  mm, and  $\mu_e = \mu_s = 0.35$ ).

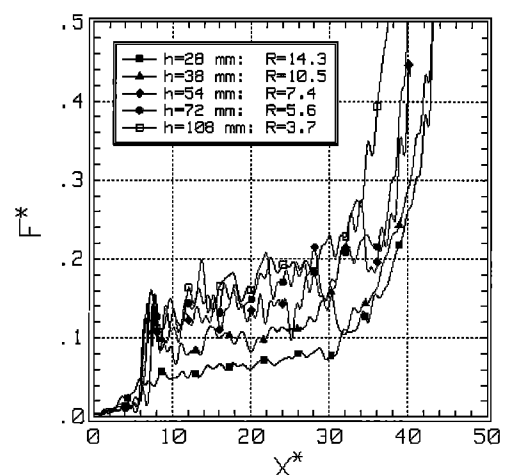


**Figure 13.** Nondimensional pusher force versus nondimensional pusher displacement for five values of the aspect ratio  $d/h$  ( $L^* = 50$ ,  $d = 400$  mm,  $w = 6$  m, and  $\mu_e = \mu_s = 0.35$ ).



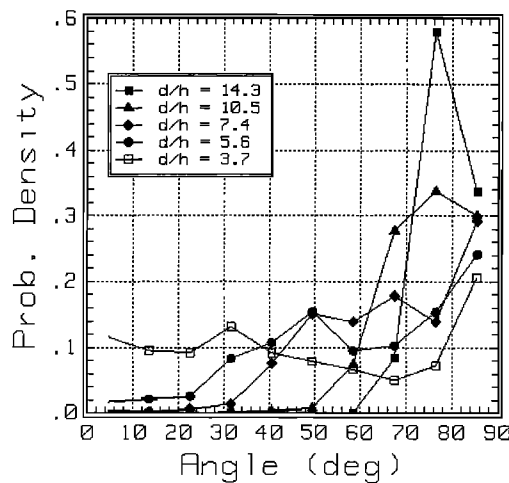


**Figure 14.** Probability density of the angle between the disk normal vectors and the horizontal plane for five values of the aspect ratio  $d/h$  at  $X^* = 32.5$  ( $L^* = 50$ ,  $d = 400$  mm,  $w = 6$  m, and  $\mu_e = \mu_s = 0.35$ ).

initial onset of failure at a nondimensional displacement of 10 in Figure 13.

The change in the strength of the surface layer is caused by the effect of the floe aspect ratio on the dynamics of the failure process. The surface layer of horizontal floes fails by overturning (Figure 1) and by rafting (Figure 2). Floes that overturn rotate, while floes that raft remain approximately horizontal. The amount of rotation that the floes undergo is indicated by the inclination of the floe normal vector to the horizontal plane. The probability density function of the inclination angle is plotted in Figure 14 for the same five values of the aspect ratio  $d/h$  used in Figure 13 at a displacement  $X^* = 32.5$ . Figure 14 shows that thin floes with large aspect ratios tend to raft (remaining horizontal), while thick floes with small aspect ratios tend to rotate. It is reasonable to conclude from Figures 13 and 14 that overturning requires higher forces than rafting.

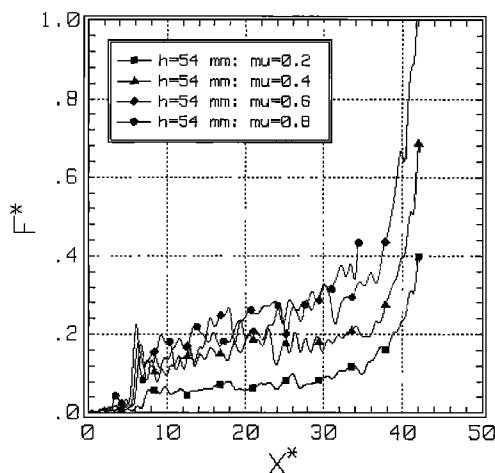


**Figure 15.** Nondimensional pusher force versus nondimensional pusher displacement for four values of the friction coefficients  $\mu_e$  and  $\mu_s$  ( $L^* = 50$ ,  $h = 54$  mm, and  $w = 6$  m).

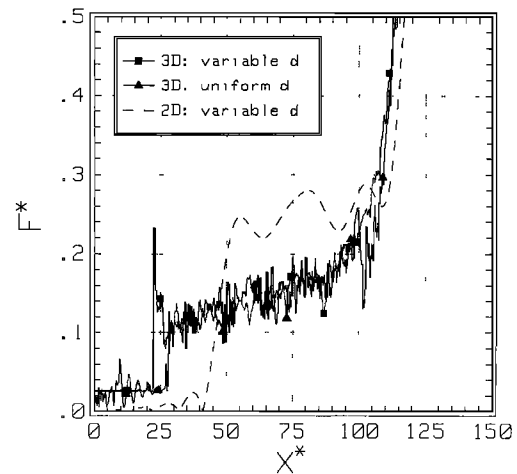


**Figure 16.** Nondimensional pusher force versus nondimensional pusher displacement from a simulation using uniform floe diameters and a simulation using the diameter to thickness distribution given in Table 2 ( $L^* = 155$ ,  $h = 54$  mm, average floe diameter  $\langle d \rangle = 193$  mm,  $w = 1.5$  m with periodic boundaries). The dashed line shows the results of a two-dimensional simulation using the polygonal discrete element model of Hopkins *et al.* [1991] with a similar set of parameters.

#### 5.4. Friction Between Floes

The effect of varying the friction coefficients is shown in Figure 15. Both the edge and surface friction coefficient were set to the indicated value. Not surprisingly, the pusher force increased with the friction coefficient.

#### 5.5. Distribution of Floe Diameters

Each of the simulations discussed in sections 4 and 5 used a single floe diameter. In Figure 16 we show the results of a simulation with a distribution of floe diameters. The floe diameters were chosen according to a floe length to thickness distribution from Keinonen and Nyman [1978] on the basis of measurements of ice blocks in Baltic pressure ridges. The distribution is shown in Table 2.

These results are compared in Figure 16 with the results of a simulation using a single floe diameter. The average floe diameter  $\langle d \rangle$  and other relevant parameters were the same in both simulations. The use of a distribution of floe diameters had no discernible effect on the results. Figure 16 also shows the smoothed results of a simulation using the two-dimensional polygonal DEM from Hopkins *et al.* [1991]. The two-dimensional simulation used the same length to thickness distribution and parameters as the three-dimensional simulation.

**Table 2.** Floe Diameter to Thickness Distribution

Floe Diameter $d/h$	Thickness Distribution $F(d/h)$
1.75	0.02
2.25	0.09
2.75	0.26
3.25	0.48
3.75	0.73
4.25	0.86
4.75	0.94
5.25	0.97
5.75	1.0

The volume of ice used in the two-dimensional simulation was the same as the ice volume per meter of channel width used in both three-dimensional simulations. The channel length and the amount of open water were also the same. However, because the floes in the two-dimensional simulation are rectangular, all of the open water in the channel must be closed before the floes reach the consolidated state, lengthening the consolidation phase. This is evident in Figure 16 where the consolidate state is reached at  $X^* = 25$  in the three-dimensional simulation and  $X^* = 45$  in the two-dimensional simulation. The forces during the compression phase are  $\sim 50\%$  higher in the two-dimensional simulation. Interestingly, the total work, which is not shown, is virtually the same in all three simulations.

## 6. Mohr-Coulomb Behavior

We have divided the deformation of a floating ice field into three phases: (1) consolidation, (2) deformation of the consolidated surface layer by overturning and rafting, and (3) continued deformation of the jumbled field of floes created during the second phase. In section 5 we have concentrated on the effects of parameter variations and boundary conditions on the forces during the second phase. The third phase of deformation is equally important in geophysical problems such as river ice jams and thickening of broken ice fields.

The traditional approach used in modeling the compression of an accumulation of ice floes is based on the assumption that the floes behave as a Mohr-Coulomb material [Pariset *et al.*, 1966; Uzuner and Kennedy, 1976]. This approach leads to the well-known equation for the force required to compress a floating layer of ice floes [Uzuner and Kennedy, 1976]

$$F = \gamma K_p H^2 \quad (6)$$

where  $H$  is the thickness of the layer. The constant  $\gamma$  and the passive pressure coefficient  $K_p$  in (6) are given by

$$\gamma = \frac{1}{2}(1 - n)\rho_i g(1 - \rho_i/\rho_w) \quad K_p = \frac{1 + \sin \phi}{1 - \sin \phi} \quad (7)$$

where  $n$  is the porosity of the layer of floes and  $\phi$  is the angle of shearing resistance. Thus a log-log graph of force versus ice layer thickness should have a slope of 2 if the ice layer deforms as a Mohr-Coulomb material.

In Figure 17 we show the results of a simulation of long duration. The diameters of the floes in the simulation were chosen according to the distribution given in Table 2. In Figure 17 the nondimensional pusher force versus the nondimensional layer thickness  $H^*$ , equal to  $H/h$ , is plotted on a log-log scale. The layer thickness  $H$  was determined by simulating the lowering of a probe from above and raising of a probe from beneath the layer of floes until the probes contacted the upper and lower surfaces of the layer. This was repeated at 1000 random locations in the floe field. The graph of force versus thickness begins at the end of the consolidation phase where the floes are floating in a single layer. The break in the slope of the graph at  $H^* \approx 2.5$  occurs at the end of the second phase of deformation. Following the break, the graph follows the dashed line, whose slope is 2. This implies that the pusher force is proportional to the square of the layer thickness and that the layer of ice floes does indeed behave as a Mohr-Coulomb material. Fitting (6) to the data using a least squares regression yields a value of 3179 for the product  $\gamma K_p$ . The porosity of the

layer of floes asymptotically approached a value between 0.35 and 0.4 at the end of the simulation. This implies a value of  $K_p$  between 10.2 and 11, which is in the range of values (9.6–12) used by Beltaos [1993] in modeling ice jams in Canadian rivers.

The average aspect ratio of the floes in the simulation discussed above was 3.56. In long-duration simulations with uniform diameter floes having average aspect ratios of 7.4 and 14.8, the floes tended to form stacks like books on a shelf during the third stage of deformation. These strong, nonisotropic floe arrangements led to a very rapid and unrealistic increase in the forces and a catastrophic failure mode that violates the Mohr-Coulomb assumption of an isotropic material in a state of uniform and continuous failure. The current computer model is unsuitable for modeling this type of deformation because it lacks failure mechanisms for floe breakage and crushing. In short, the applicability of Mohr-Coulomb failure theory to an assembly of ice floes depends on the floe aspect ratio and needs to be further explored.

## 7. Conclusions

The compression of circular ice floes in a rectangular channel has been studied using computer simulations. The simulations began with a single layer of circular floes floating horizontally at the water surface in a rectangular channel. The floes were compressed by a pusher plate moving at a constant speed. We divided deformation into three phases: (1) consolidation, (2) deformation of the consolidated surface layer by overturning and rafting, and (3) continued deformation of the jumbled field of floes created during the second phase. The accuracy of the simulations was verified by directly comparing force versus displacement curves from the simulations with the results of similar model experiments performed in a refrigerated basin at the Ship Laboratory of the Helsinki University of Technology. The dimensions and parameters used in the simulations were measured from the model experiments. Further

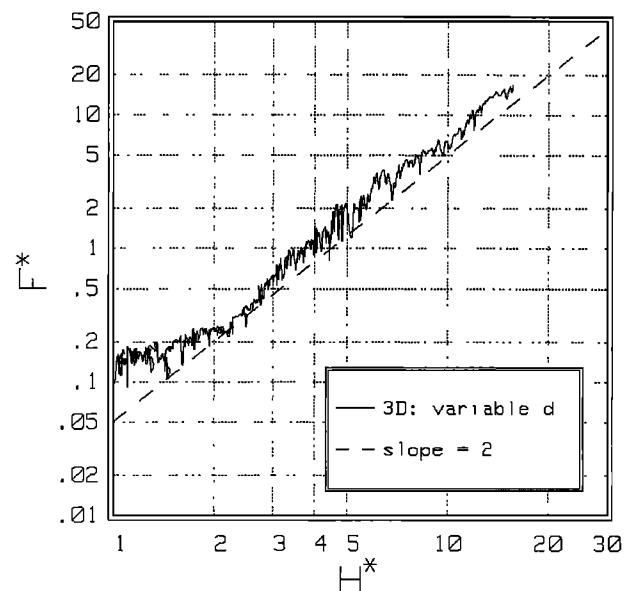


**Figure 17.** Nondimensional pusher force versus nondimensional rubble layer thickness  $H^*$  for floes with diameter to thickness distribution given in Table 2 ( $L^* = 313.5$ ,  $h = 54$  mm,  $\langle d \rangle = 193$  mm, and  $w = 1.5$  m with periodic boundaries).

simulations were performed to determine the effects of varying parameters and boundary conditions on the force versus displacement curves.

Two general factors were found to determine the force levels in the second phase of deformation. The first is the compressive strength of the surface layer of floes. The surface layer of floes fails either by rafting, by overturning, or by a combination of the two. The tendency to favor one mechanism over the other is affected by the aspect ratio of the disks and the friction coefficient between the disks. Thick or rough disks tend to overturn, while thin or smooth disks tend to raft. The simulations showed that a low aspect ratio or a high friction coefficient, which favored overturning over rafting, strengthened the surface layer and led to higher forces. The second factor is the boundary condition imposed by the lateral confinement of the floes by the sheets on each side of the channel. The frictional force at the channel edges creates a gradient in the longitudinal force transmitted through the floe field with the greatest forces occurring at the pusher. The gradient causes initial failure to occur in the vicinity of the pusher. The rubble in front of the pusher thickens progressively as the leading edge of the failure zone propagates toward the opposite end of the channel. This progressive thickening results in an apparently linear increase in the force versus displacement graphs. The effects of lateral confinement diminish with increasing channel width. In channels without edge friction (modeled using periodic boundaries), failure occurs sporadically throughout the channel. In this case, forces remain roughly constant until the entire initial surface layer of floes has failed. In both cases the force rises steeply when the failure zone reaches the end of the channel. The effect of the frictional force at the channel edges on the longitudinal force gradient shares similarities with viscous drag forces in geophysical problems such as water flowing beneath a river ice accumulation or an onshore wind pushing an ice field against stationary ice. In these cases the initial failure and the thickest ice accumulation would occur at the downstream or downwind end of the accumulation.

Finally, we performed several long-duration simulations to determine whether or not the floating layer of circular ice floes behaved like a Mohr-Coulomb material during the third phase of deformation. This was found to depend on the aspect ratio of the floes, with low aspect ratio floes behaving like a Mohr-Coulomb material, while high aspect ratio floes tended to stack like books on a shelf. This strong, nonisotropic floe arrangement led to a very rapid and unrealistic increase in the forces and a catastrophic failure mode that violates the Mohr-Coulomb assumption of an isotropic material in a state of uniform and continuous failure.

**Acknowledgments.** The work described here is a part of the Ice State project supported by the European Commission through the Marine Science and Technology program (MAST III). The participants in the project are Helsinki University of Technology, Nansen Environmental and Remote Sensing Center, Scott Polar Research Institute, University of Helsinki, and University of Iceland. Mark Hopkins's work on this project, during a year spent at the Helsinki Uni-

versity of Technology, was supported by the U.S. Army through a Secretary of the Army Research and Study Fellowship and by the Finnish Maritime Foundation. Steven F. Daly and Walter B. Tucker made many suggestions which improved the manuscript.

## References

- Babic, M., H. T. Shen, and G. Bedov, Discrete element simulations of river ice transport, paper presented at Ice Symposium, Int. Assoc. for Hydraul. Res., Espoo, Finland, 1990.
- Beltaos, S., Numerical computation of river ice jams, *Can. J. Civ. Eng.* 20(1), 88–99, 1993.
- Evans, D. J., and S. Murad, Singularity free algorithm for molecular dynamics simulation of rigid polyatomics, *Mol. Phys.* 34(2), 321–326, 1977.
- Hansen, E. H., and J. Tuhkuri, Ice tank tests on marginal ice zone rheology, in *Proceedings of the 16th International Conference on Off-shore Mechanics and Arctic Engineering: Arctic/Polar Technology*, vol. 4, edited by H. Yamaguchi et al., pp. 469–475, Am. Soc. of Mech. Eng., New York, 1997.
- Hopkins, M. A., On the ridging of an intact sheet of lead ice, *J. Geophys. Res.*, 99, 16351–16360, 1994.
- Hopkins, M. A., and W. D. Hibler III, Numerical simulations of a compact convergent system of ice floes, *Ann. Glaciol.*, 15, 26–30, 1991.
- Hopkins, M. A., and M. Y. Louge, Inelastic micro-structure in rapid granular flows of smooth disks, *Phys. Fluids A*, 3(1), 47–57, 1991.
- Hopkins, M. A., W. D. Hibler III, and G. M. Flato, On the numerical simulation of the sea ice ridging process, *J. Geophys. Res.*, 96, 4809–4820, 1991.
- Hopkins, M. A., S. F. Daly, and J. H. Lever, Three-dimensional simulation of river ice jams, paper presented at the 8th International Specialty Conference on Cold Regions Engineering, Am. Soc. of Civ. Eng., Fairbanks, Alaska, Aug. 12–17, 1996.
- Keinonen, A., and T. Nyman, An experimental model-scale study on the compressible frictional and cohesive behaviour of a broken ice mass, paper presented at Symposium on Ice Problems, Int. Assoc. for Hydraulic Res., Delft, Netherlands, 1978.
- Loset, S., Discrete element modelling of a broken ice field, II, Simulation of ice loads on a boom, *Cold Reg. Sci. Technol.*, 22, 349–360, 1994.
- Pariset, E., R. Hausser, and A. Gagnon, Formation of ice covers and ice jams in rivers, *J. Hydraul. Div. Am. Soc. Civ. Eng.*, 92, 1–24, 1966.
- Sayed, M., M. Serrer, and D. A. Arden, Numerical simulations of ice jams in Lake St. Peter, *Tech. Rep. IECE-CRT-CTR-004*, Nat. Res. Council, Ottawa, Canada, 1994.
- Serra, J., Introduction to mathematical morphology, *Comput. Vision Graphics Image Process.*, 35, 283–305, 1986.
- Tuhkuri, J., and M. Lensu, Ice tank tests on rafting of a broken ice field, *Ship Lab. Rep. m-218*, Helsinki Univ. of Technol., Espoo, Finland, 1997.
- Uzuner, M. S., and J. F. Kennedy, Theoretical model of river ice jams, *J. Hydraul. Div. Am. Soc. Civ. Eng.*, 102, 1365–1383, 1976.
- Walton, O. R., and R. L. Braun, Simulation of rotary-drum and repose tests for frictional spheres and rigid sphere clusters, paper presented at Joint DOE/NSF Workshop On Flow of Particulates and Fluids, Dep. of Energy, Ithaca, N. Y., Sept. 29 to Oct. 1, 1993.
- White, F. M., *Fluid Mechanics*, McGraw-Hill, New York, 1979.

M. A. Hopkins, U.S. Army Cold Regions Research and Engineering Laboratory, 72 Lyme Road, Hanover, NH 03755. (hopkins@crrel.usace.army.mil)

J. Tuhkuri, Ship Laboratory, Helsinki University of Technology, Tietotie 1, 02150 Espoo, Finland.

(Received April 15, 1998; revised March 5, 1999; accepted April 15, 1999.)